DIRECT NUMERICAL SIMULATION OF CONJUGATE TURBULENT HEAT TRANSFER IN POROUS SQUARE DUCT

Y. Kuwata, K. Tsuda and K. Suga
Department of Mechanical Engineering,
Osaka Prefecture University
Sakai, Osaka 599-8531, Japan.
kuwata@me.osakafu-u.ac.jp

ABSTRACT

Turbulent conjugate heat transfer of air flow through a duct partially filled with aluminum porous material is studied by means of the lattice Boltzmann direct numerical simulation. The constant wall temperatures are imposed to the top and bottom walls with a temperature difference, while the adiabatic boundary conditions are applied to the lateral side walls. In addition to turbulent heat transfer of the air flow, the heat conduction of the porous material is simultaneously solved. Despite the confinement by the lateral side walls, the large-scale transverse wavy motion due to the Kelvin-Helmholtz instability is developed just over the porous wall. It is found that the intensified turbulence over the porous wall due to the relaxation of the wall-blocking effect significantly enhances the secondary flow, and the advection by the enhanced secondary considerably contributes to the heat transfer near the top wall. In contrast, the heat transfer near the porous wall interface is dominated by the turbulent transport. Analyzing the volume and Reynolds averaged energy equation, we confirm that the heat flux term due to the mean velocity dispersion considerably contributes to the heat transfer deeply inside the porous wall while the advection by the macroscopic velocity induced by the penetrating secondary flow is significant near the porous interface.

INTRODUCTION

Since porous media have large contact area per volume leading to high heat and mass transfer performance, various applications of the porous materials can be found in engineering devices, e,g., the carbon paper for gas diffusion layer of fuel cells; the metal foam, sphere packing, rod bundles for heat exchangers. In the flows around porous material, the flow transition from laminar to turbulent occurs at relatively low-Reynolds number due to flow disturbance induced by the complicated porous geometry (Dybbs & Edwards, 1984). In order to understand turbulent heat transfer mechanisms of such flows based on high fidelity information that cannot be accessed by experimental investigations, many numerical studies have been carried out. However, most of the numerical studies applied Reynolds-averaged Navier-Stokes (RANS) turbulence models with macroscopic porous medium models: pipe flows filled with porous materials (Yang & Hwang, 2009), flows through porous materials bounded by solid walls (Saito & de Lemos, 2010). Moreover, eddy resolving simulations studies are

limited to simple flow geometries: fully-developed porous medium flows (Suga *et al.*, 2017) and and porous-walled channel flows (Chandesris *et al.*, 2013). It is well known that turbulence over a porous wall is enhanced due to weakened wall-blocking effect, thus leading to an increase in wall friction (Suga *et al.*, 2010; Breugem *et al.*, 2006); however, the effect of a porous wall on an engineering turbulent flow have yet to be studied. Accordingly, as a first attempt, we focus on a rectangular duct flow which has relatively simple configuration but has great engineering interest owing to the existing of secondary flows. Performing the direct numerical simulation of the conjugate heat transfer in a rectangular duct partially filled with porous material, we aim to reveal the influence of the porous medium on the turbulent heat transfer in the clear flow region. In addition, the transport mechanism inside the porous medium is discussed from a macroscopic viewpoint by analyzing the budget terms in the volume and Reynolds averaged energy equations.

Numerical scheme

The lattice Boltzmann method (LBM) has achieved considerable success in large-scale complex flow simulations owing to the simplicity of the wall treatment, nature of its low numerical dissipation and dispersion, and high performance of parallel computing. The lattice Boltzmann equation can be obtained by discretizing the velocity space of the Boltzmann equation into a finite number of discrete velocities $\xi_\alpha \{\alpha = 0, \cdots, Q-1\}$. In the case of the LBM, there are several choices for discrete velocity models and collision term models. We select the D3Q27 multiple-relaxation-time LBM (MRT-LBM) developed by Suga *et al.* (2015) to simulate a time-dependent flow, which was rigorously validated in the application to the DNS of a turbulent channel flow (Suga *et al.*, 2015) and applied to the DNS of turbulent flows over rough and porous walls (Kuwata & Suga, 2016, 2017).

The time evolution of the distribution function of the MRT-LBM can be written as

$$|f(r_i + \xi_\alpha \delta t, t + \delta t)\rangle - |f(r_i, t)\rangle = -M^{-1}\hat{S}[m(r_i, t) - m^{eq}(r_i, t)], \quad (1)$$

where $|f\rangle = (f_0, f_1, \cdots, f_{26})^T$, δt denotes the time step, and ξ_α represents the discrete velocity vectors. The matrix M is

a 27×27 matrix which linearly transforms the distribution functions to the moments $|m\rangle = M|f\rangle$. The collision matrix $\hat{S}$ is diagonal:

$$\hat{S} \equiv diag(0,0,0,0,s_4,s_5,s_5,s_7,s_7,s_7,s_{10},s_{10},s_{10},s_{13},$$
$$s_{13},s_{13},s_{16},s_{17},s_{18},s_{18},s_{20},s_{20},s_{20},s_{23},s_{23},s_{23},s_{26}). \quad (2)$$

A set of the relaxation parameters is as follows:

$$s_4 = 1.54, \quad s_5 = s_7, \quad s_{10} = 1.5, \quad s_{13} = 1.83, \quad s_{16} = 1.4,$$
$$s_{17} = 1.61, \quad s_{18} = s_{20} = 1.98, \quad s_{23} = s_{26} = 1.74. \quad (3)$$

The relaxation parameters s_5, s_7 are related to the kinematic viscosity ν,

$$\nu = c_s^2 \left(\frac{1}{s_5} - \frac{1}{2} \right) \delta t = c_s^2 \left(\frac{1}{s_7} - \frac{1}{2} \right) \delta t. \quad (4)$$

For the scaler fields, there are also several discrete velocity models and collision term models as with the flow field models. After validation test in a flow around a bluff body, a turbulent channel flow, and turbulent porous medium flows, we confirm the D3Q19 discrete velocity model with the regularized collision term model yields a reasonable prediction (Suga *et al.*, 2017). The time evolution of the particle distribution function is expressed as follows:

$$|g(r_i + e_\alpha \delta t, t + \delta t)\rangle = |g^{(eq)}(r_i, t)\rangle + \left(1 - \frac{1}{\tau_g} \right) |g'(r_i, t)\rangle, \quad (5)$$

where the notation $|g\rangle = (f_0, f_1, \cdots, f_{18})^T$, e_α represents the discrete velocity vectors. The terms $g^{(eq)}$ and $|g'(r_i, t)$ are the equilibrium distribution function and regularized non-equilibrium part of the distribution function, respectively. The equilibrium distribution function is expressed as follows:

$$g_\alpha^{(eq)} = w_\alpha T \left(1 + \frac{u \cdot e_\alpha}{c_s^2} \right), \quad (6)$$

where temperature is $T = \Sigma_\alpha g_\alpha$, and u is the fluid velocity. The regularized non-equilibrium part of the distribution function $|g'(r_i, t)$ is

$$g_\alpha' = w_\alpha \sum_{n=0}^{N} \left(\frac{1}{n!} C^{(n)} \mathbf{H}^{(n)}(e_\alpha/c_s) \right), \quad (7)$$

For the D3Q19 model, the Hermite expansion coefficients $C^{(n)}$ and the Hermite polynomial $\mathbf{H}^{(n)}$ are

$$C^{(n)} = \sum_\alpha g_\alpha^{(neq)} \mathbf{H}^{(n)}(e_\alpha/c_s), \quad (8)$$

$$\mathbf{H}^{(0)}(e_\alpha/c_s) = 1, \quad (9)$$

$$\mathbf{H}_i^{(1)}(e_\alpha/c_s) = \frac{e_{\alpha,i}}{c_s}, \quad (10)$$

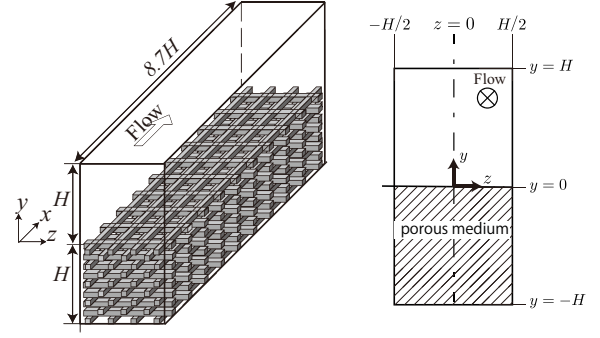$$\mathbf{H}_i^{(2)}(e_\alpha/c_s) = \frac{e_{\alpha,i} e_{\alpha,j}}{c_s^2}. \quad (11)$$
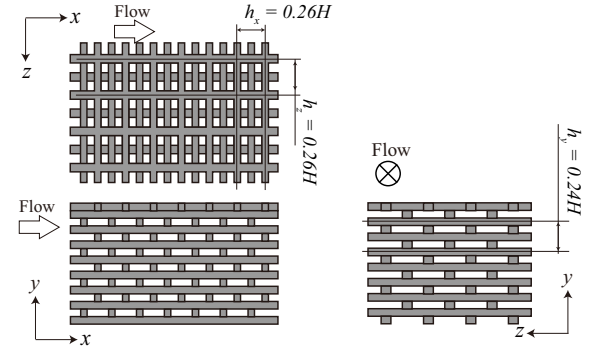

Figure 1. Computational geometry of a porous duct flow.

Figure 2. Sketch of a porous medium geometry

The thermal diffusivity Γ is related to the relaxation time τ_g as follows:

$$\Gamma = c_s^2 \left(\tau_g - \frac{1}{2} \right) \delta t. \quad (12)$$

It should be noted that, unlike the other Navier–Stokes solvers, the LBM does not require any special treatment for simulating the conjugate heat transfer, which enables us to easily perform conjugate heat transfer in complicated flow geometries.

Flow conditions

Figures 1 illustrates the computational geometry of a rectangular duct flow partially filled with porous material. The rectangular duct size is $8.7H(x) \times 2H(y) \times H(z)$, and a porous medium consisted of staggered square bar arrays as illustrated in Fig.2 is considered in the lower half of the rectangular duct $-1 < y/H < 0$; thus, the cross-section of the clear flow region is square. The periodic boundary conditions are applied in the streamwise direction, and the flow is driven by imposing a streamwise pressure difference. The Reynolds number based on the bulk mean velocity in the clear fluid region U_b and the duct width H is 3500, and the resulting friction Reynolds number over the porous wall, defined as $\text{Re}_\tau = u_\tau H/\nu$ with u_τ being the friction velocity at the porous wall, is 395. The friction velocity u_τ is computed from a relation among pressure drop, wall-shear stress at the solid walls, and that at the porous wall. For the thermal boundary conditions, the top $(y = H)$ and bottom $(y = -H)$ walls are assumed to

be constant with a temperature difference ΔT ($\Delta T > 0$) as $T_{y=H} = T_{y=0} + \Delta T$, while an adiabatic wall is considered to the lateral walls at $z/H = -0.5, 0.5$. The fluid Prandtl number is set to $Pr = 0.71$, and we consider the conjugate heat transfer: a thermal diffusivity ratio between the solid and fluid phases is 4.4, which corresponds to a ratio between aluminum and air. The porosity of the porous medium is 0.77, and the permeability Reynolds number based on the streamwise wall-permeability is $Re_K = u_\tau \sqrt{K}/\nu = 7.3$. In this permeability Reynolds number flow, the wall permeability of a porous wall significantly affect turbulence because the wall-blocking effect is weakened (Suga *et al.*, 2010). The grid node number is $3328(x) \times 770(y) \times 402(z)$, and 23×23 grids are used to resolve a cross-section of a square bar. The computational grid is equilateral, and the resolution normalized by the porous wall unit velocity is 1.0, which is comparable to those employed in the lattice Boltzmann DNS studies Kuwata & Suga (2016, 2017). As the simulated flow is fully developed, the Reynolds averaged values are further averaged in the streamwise direction. Although the flow inside the porous medium is inhomogeneous in the streamwise direction, the fluid phase spatial averaging in the streamwise direction is applied to the values inside the porous medium region of $y/H < 0$.

Results and discussion

To validate the simulation results, Fig. 3 compares the simulated mean velocity U and Reynolds shear stress $-\overline{u'v'}$ with the measured data in our laboratory in the symmetry plane of $y/H = 0.0$. For a comparison, the result of the porous-walled channel flow from Kuwata & Suga (2016) is also plotted in Fig. 3. We can confirm an excellent agreement with the experimental results, which demonstrates that the present DNS can provide high fidelity information. The Reynolds shear stress is considerably enhanced over the porous wall, primarily resulting from the relaxation of the wall-blocking effects as reported by Suga *et al.* (2010). Moreover, as can be observed in the streamwise velocity fluctuations in Fig.4, the turbulent vortex structure is modified by the permeable porous wall. The streamwise elongated streaky structure is developed below the top solid wall, whereas the development of the streaky structure is prevented over the porous wall. The high- and low-speed regions, which have the strong coherence in the spanwise direction, alternatively appear in the streamwise direction. Similar observations were made in the DNS studies of a turbulent porous-walled channel flow (Breugem *et al.*, 2006; Kuwata & Suga, 2016), and they reported the transverse wavy motion was originated from the Kelvin-Helmholtz type of instability initiated at the inflection point of the streamwise velocity just over the porous wall. The above mentioned effects of the porous wall on turbulence are consistent with the previous studies of porous-walled channel flows (Suga *et al.*, 2010; Breugem *et al.*, 2006; Kuwata & Suga, 2016); however, unlike the result of the porous-walled channel flow in Kuwata & Suga (2016), Fig. 3 (a) shows that a maximum peak point of the streamwise mean velocity does not shit toward the top wall, and the predicted mean velocity profile deviates largely from that of turbulent porous-walled channel flow. The difference can be attributed to the influence of the secondary flow which is well known to be induced in the rectangular duct flow system.

In order to see the mean velocity distributions in the cross-section, Fig. 5 shows the contour maps of the stream-
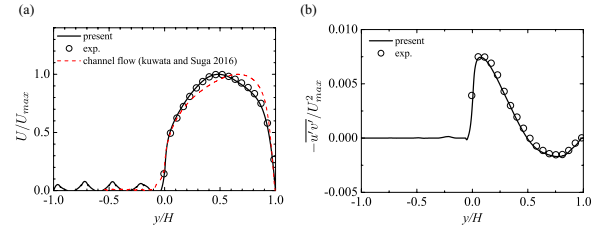

Figure 3. Comparison of the simulated results with the experimental data in the symmetry plane: (a) mean velocity together with the porous-walled channel flow results in Kuwata & Suga (2016), (b) Reynold shear stress.
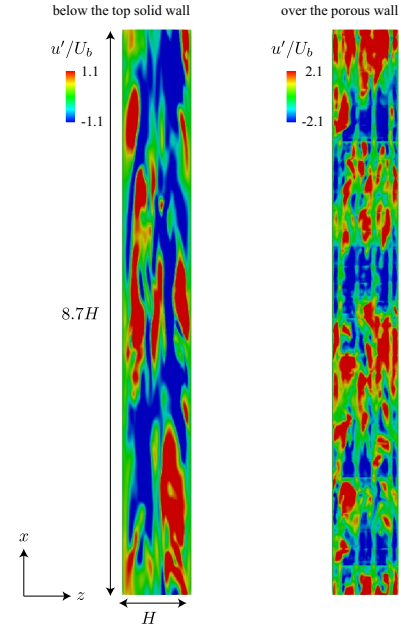

Figure 4. Streamwise velocity fluctuations below the top solid wall at $y = H$ and over the porous wall at $y = 0$.

wise mean velocity U/U_b and the secondary flow intensity $\sqrt{V^2 + W^2}/U_b$ along with the cross-streamwise velocity vectors in the clear fluid region. Here, the values denoted by the capital stand for the averaged values. In a square duct flow confined by the impermeable solid walls, the counter-rotating eight vortices which convects the high momentum fluid from the core region to the corner regions, leading to the distortion of the streamwise mean velocity (Huser & Biringen, 1993). These counter-rotating eight vortices are absent in the porous duct as observed in Fig.5(b), and quite different secondary flow pattern is formed. In Fig.5(b), the mean secondary flow from the core region toward the corners is present in the bottom corners but is absent in the top corners. The secondary flow toward the bottom corners generates the counter-clockwise rotating flow sitting on the porous wall and induces the upward flow along the lateral walls located at $z/H = -0.5, 0.5$. The upward flow reaches near the top wall at $y/H = 1.0$, and this prevents the formation of the counter-rotating vortex pair in the top corners. In the symmetry plane at $z/H = 0$, the downward flow is induced and convects the low momentum fluid near the top wall toward the core region, resulting in the hollowed out mean velocity velocity in Fig.5 (b): the low speed region below the top solid wall $y/H = 1.0$ near the symmetry plane of $z/H = 0.0$ is directed toward the core region. On the

other hand, since the intensity of the secondary flow toward the bottom corners is not significant compared with that of the downward flow near the symmetry plane, the distortion of the streamwise mean velocity directed toward the bottom corners is insignificant. The secondary flow intensities of the upward flow along the lateral walls and the downward from in the symmetry plane particularly increase in strength. The maximum value of the secondary flow intensity reaches 6% of the bulk mean velocity, which is considerably greater than that observed in a square duct (Huser & Biringen, 1993).

Figure 6 shows the contour maps of the temperature distributions. To better visualize the convection heat transfer by the enhanced secondary flow, the heatlines proposed by Kimura & Bejan (1983) are also shown in the figure. The heatlines defined in analogy with streamlines are expressed as the iso-contour line of heat function H, defined as follows:

$$\frac{\partial H}{\partial y} = \rho W c_p (T - T_0) - k\frac{\partial T}{\partial z}$$
$$\frac{\partial H}{\partial z} = \rho V c_p (T - T_0) - k\frac{\partial T}{\partial y} \qquad (13)$$

where c_p, k and T_0 are the constant pressure specific heat, thermal conductivity, and reference temperature, respectively. The reference temperature are determined as $T_0 = T_{y=H}$ and $T_0 = T_{y=0}$ to compute the heat functions in the clear flow region and in the porous medium region, respectively. The above definition, which is similar to the stream function for the streamlines, suggests that heat is transferred along heatlines due to the combined effects of the conduction and the convection. If heat transfer is dominated by conduction, heatlines are orthogonal to isothermal lines.

Figure 6 (a) confirms that the heatlines in the clear fluid region considerably reflect the secondary flow pattern as shown in Fig.5 (b); therefore, the heat in the clear flow region is convected by the secondary flows rather than the conduction. Indeed, it can be clearly observed from Figs.5(b) and 6(a) that the upward mean flow along the lateral walls convects the high temperature fluid to the top wall, and the downward flow in the symmetry plane convects the low temperature fluid toward the core region. Since a spacing between the heatlines corresponds to the intensity of the heat transfer, the convective heat transfer due to the downward flow in the symmetry plane is found to be significant. In contrast, when we focus in the porous medium region in Fig.6(b), the heatlines exhibit a recirculating pattern in the pore region, resulting from the cross-streamwise mean velocity dispersion. This observation suggests that not only the heat conduction but also the advection largely contributes to the heat transfer deep inside the porous medium.

The heat transfer mechanism in the clear fluid region is discussed by analyzing the budget terms of the normalized energy equation by U_b,H and (ΔT):

$$0 = -V\frac{\partial T}{\partial y} - W\frac{\partial T}{\partial z} - \frac{\partial \overline{v'T'}}{\partial y} - \frac{\partial \overline{w'T'}}{\partial z}$$
$$+ \frac{1}{PrRe_b}\left(\frac{\partial^2 T}{\partial y^2} + \frac{\partial^2 T}{\partial z^2}\right), \qquad (14)$$

where the terms $-V\frac{\partial T}{\partial y}$ and $-W\frac{\partial T}{\partial z}$ denote the vertical and horizontal advection terms, respectively. The term
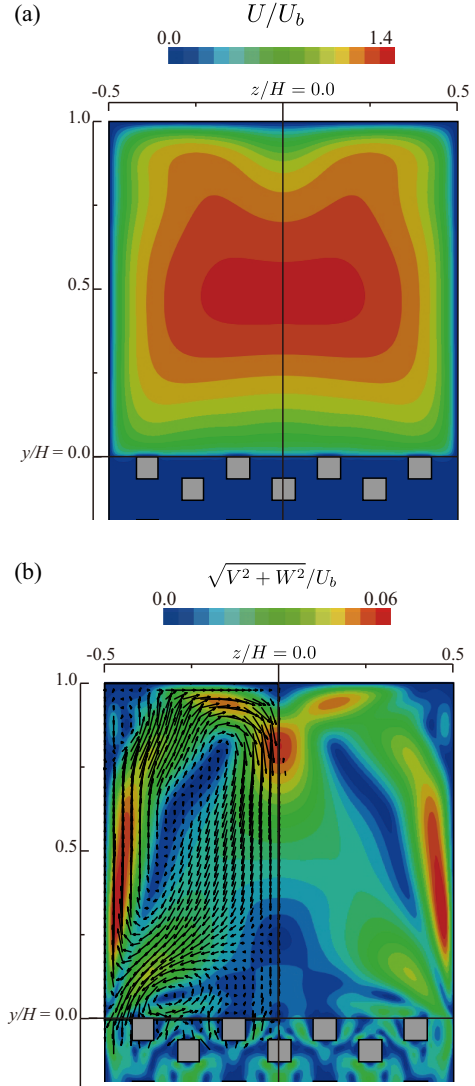

(a) U/U_b

(b) $\sqrt{V^2 + W^2}/U_b$

Figure 5. Contour map of the mean velocity distribution: (a) streamwise mean velocity, (b) Intensity of cross-streamwise mean velocity with velocity vectors.

$-\frac{\partial \overline{v'T'}}{\partial y} - \frac{\partial \overline{w'T'}}{\partial z}$ is the turbulent transport and the last term on the right-hand side is the conduction term. The budget term profiles near the lateral wall at $z/H = -0.375$ and those in the symmetry plane at $z/H = 0.0$ are respectively presented in Fig.7(a) and (b). In Fig.7(a), near the lateral walls, the vertical turbulent transport and advection terms convect the low temperature fluid toward the top wall. The contribution by the turbulent transport is confined near the top wall $0.8 < y/H < 1.0$ while the vertical advection, which is due to the upward secondary flow, considerably contributes in the upper half of the clear fluid region $0.5 < y/H < 1.0$. The convection toward the top wall increases the temperature gradient near in the vicinity of the top wall as observed in Fig.6(a), thus resulting in a significant increase in the heat conduction in the region. The heat transfer near the porous wall is dominated by the turbulent transport; however, the budget terms near the porous wall have smaller magnitudes than those near the top wall. In the upper half of the clear fluid region $0.5 < y/H < 1.0$ in the symmetry plane, Fig.7(b) confirms that the transported energy by the horizontal turbulent heat flux is convected by the advection due to the downward secondary flow. In contrast, near the
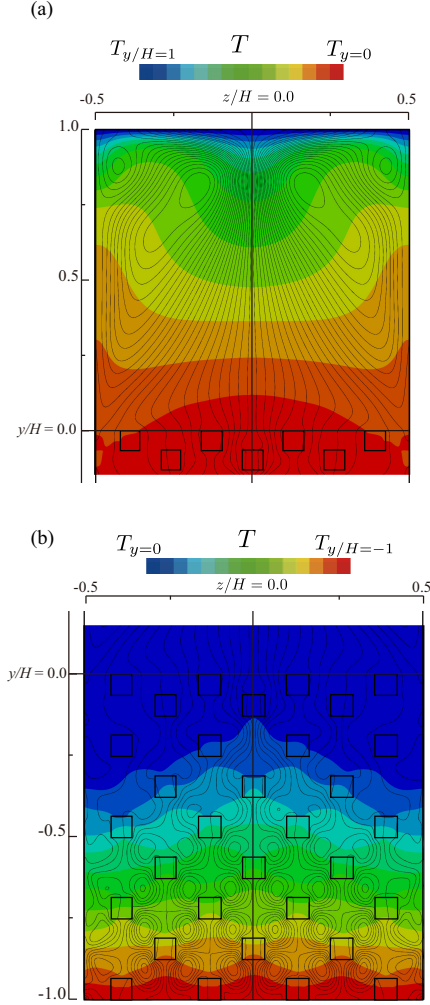
(a)

(b)

Figure 6. Contour map of the mean temperature distribution with heatlines: (a) clear flow region, (b) inside the porous medium.

porous wall region, as the porous wall enhances turbulent velocity fluctuation, the wall-normal turbulent heat flux is particularly enhanced over the porous medium and dominantly transport the energy.

Finally, we discuss the heat transfer mechanism in the porous medium region from a macroscopic viewpoint. Applying the volume and Reynolds averaging, we can obtain the double (volume and Reynolds) averaged energy equation normalized by U_b, H and ΔT as follows:

$$
0 = \underbrace{-\varphi \langle U_j \rangle \frac{\partial \langle T \rangle}{\partial x_j}}_{C} + \underbrace{\frac{1}{PrRe_b} \frac{\partial}{\partial x_j} \left(\frac{\partial \varphi \langle T \rangle}{\partial x_j} + \frac{1}{\Delta V} \int_A n_j T dA \right)}_{D}
$$
$$
\underbrace{- \frac{\partial}{\partial x_j} \varphi \overline{\langle u'_j T'_f \rangle}}_{T} \underbrace{- \frac{\partial}{\partial x_j} \varphi \langle \tilde{\bar{u}}_j \tilde{T} \rangle}_{\mathscr{D}} + \underbrace{\frac{1}{PrRe_b \Delta V} \int_A n_j \frac{\partial T}{\partial x_j} dA}_{S_w},
$$
(15)

where $\langle \phi \rangle$ is the volume-averaged value of a variable ϕ, and $\tilde{\phi}$ denotes the dispersion: $\tilde{\phi} = \phi - \langle \phi \rangle$. The representative volume of the spatial averaging is, $\Delta V = 8, 7H(x) \times h_y(y) \times h_z(z)$, and φ, A and n_j are the porosity, superficial area of

the solid phase, and its unit normal vector pointing outward from the fluid to the solid phase, respectively. The budget terms C and D are the advection by the macroscopic velocity and molecular diffusion, respectively. The terms T and $\mathscr{D}$ stand for the transport terms by the volume averaged turbulent heat flux and dispersion heat flux, respectively. Surface integration term included in D is the tortuosity term, and the wall-heat transfer term S_w acts as an energy exchange term between the solid and fluid phases. Profiles of those budget terms in the symmetry plane are presented in Fig.8. The heat conduction and dispersion transport terms are found to be balanced near the most bottom wall. The advection by the macroscopic mean velocity $\langle U_j \rangle$ increases as it separates from the bottom wall. The turbulence and dispersion transport terms considerably contribute below the porous medium ($-0.4 < y/H < 0.0$), and they are almost balanced with the advection by the macroscopic mean velocity. The enhanced turbulent transport is due to the turbulence penetration whereas the secondary flow in the clear flow region penetrate the porous wall, and this increases the transport terms by the macroscopic mean velocity and mean velocity dispersion. Contribution of the wall-heat transfer term is found to be marginal, thus indicating that the solid and fluid phase temperatures nearly reach an equilibrium temperature and the heat transfer between the solid and fluid phase hardly occurs.

Conclusions

To discuss the effects of the porous wall on turbulent heat transfer in a duct flow, we carried out direct numerical simulation of turbulent conjugate heat transfer of an air flow through a rectangular duct partially filled with aluminum porous material. We consider the constant wall temperatures to the top and bottom walls with a temperature difference, while the adiabatic boundary conditions are applied to the lateral walls. The heat conduction of the aluminum porous medium is simultaneously simulated. As in a turbulent boundary layer over a porous wall, the large-scale transverse wavy motion induced by the Kelvin-Helmholtz instability is developed just over the porous wall, and the turbulence over the porous wall is significantly enhanced due to the weakened wall blocking. Moreover, the enhanced turbulence strengthens the secondary flow, which substantially affects the mean velocity profile. The budget term analysis of the energy equation suggests that the enhanced secondary flow dominantly transports energy near the top wall whereas the heat transfer near the porous wall is dominated by the turbulent transport. Analyzing the volume and Reynolds averaged energy equation, we confirm that the velocity dispersion dominantly transports the energy deep inside the porous wall, whereas the penetration of the turbulence and secondary flow into the porous wall increases the heat transfer just below the porous interface.

REFERENCES

Breugem, W. P., Boersma, B. J. & Uittenbogaard, R. E. 2006 The influence of wall permeability on turbulent channel flow. *J. Fluid Mech.* **562**, 35–72.

Chandesris, M., d'Hueppe, A., Mathieu, B., Jamet, D. & Goyeau, B. 2013 Direct numerical simulation of turbulent heat transfer in a fluid-porous domain. *Phys, Fluids* **25** (12), 125110.
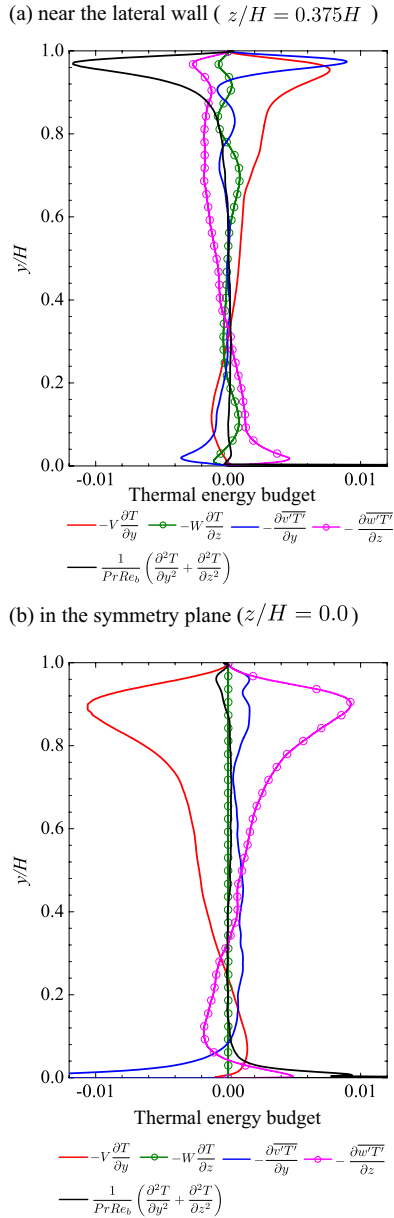
Dybbs, A. & Edwards, R. V. 1984 A new look at porous me-

(a) near the lateral wall ($z/H = 0.375H$)

(b) in the symmetry plane ($z/H = 0.0$)

Figure 7. Profiles of the thermal budget terms: (a) near the lateral walls at $z/H = 0.375$, (b) in the symmetry plane $z/H = 0.0$.
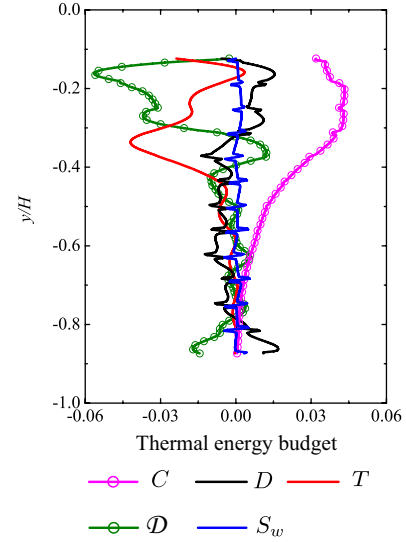

Figure 8. Profiles of the double averaged thermal budget terms of Eq.(15) in the symmetry plane $z/H = 0.0$: C advection by the macroscopic velocity, D molecular diffusion, T turbulent transport, $\mathcal{D}$ dispersion transport, and S_w the wall-heat transfer term.

of convective heat transfer. *J. heat transfer* **105** (4), 916–919.

Kuwata, Y & Suga, K 2016 Lattice boltzmann direct numerical simulation of interface turbulence over porous and rough walls. *Int. J. Heat Fluid Flow* **61**, 145–157.

Kuwata, Y. & Suga, K. 2017 Direct numerical simulation of turbulence over anisotropic porous media. *J. Fluid Mech.* **831**, 41–71.

Saito, Marcelo B. & de Lemos, Marcelo J.S. 2010 A macroscopic two-energy equation model for turbulent flow and heat transfer in highly porous media. *Int. J. Heat Mass Transfer* **53** (11), 2424 – 2433.

Suga, K., Chikasue, R. & Kuwata, Y. 2017 Modelling turbulent and dispersion heat fluxes in turbulent porous medium flows using the resolved les data. *Int. J. Heat Fluid Flow* **68**, 225 – 236.

Suga, K., Kuwata, Y., Takashima, K. & Chikasue, R. 2015 A D3Q27 multiple-relaxation-time lattice Boltzmann method for turbulent flows. *Comput. Math. Appl.* **69**, 518–529.

Suga, K., Matsumura, Y., Ashitaka, Y., Tominaga, S. & Kaneda, M. 2010 Effects of wall permeability on turbulence. *Int. J. Heat Fluid Flow* **31**, 974–984.

Yang, Yue-Tzu & Hwang, Ming-Lu 2009 Numerical simulation of turbulent fluid flow and heat transfer characteristics in heat exchangers fitted with porous media. *Int. J. Heat Mass Transfer* **52** (13), 2956 – 2965.

dia fluid mechanics-Darcy to turbulent. In *Fundamentals of Transport Phenomena in Porous Media* (ed. J. Bear & M. Y. Corapcioglu), *NATO ASI Series*, vol. 82, pp. 199–256. Springer Netherlands.

Huser, A. & Biringen, S. 1993 Direct numerical simulation of turbulent flow in a square duct. *J. Fluid Mech.* **257**, 65–95.

Kimura, S. & Bejan, A. 1983 The " heatline " visualization